Huixing Zhang, Clara Lana Fidelis, Michaela Wilhelm, Zhipeng Xie, Kurosch Rezwan

Macro/mesoporous SiOC ceramics of anisotropic structure for cryogenic engineering

Recommended Citation (primary publication/Version of Record) incl. DOI:

Take down policy

Macro/mesoporous SiOC ceramics of anisotropic structure for cryogenic engineering

Huixing Zhang [a], Clara Lana Fidelis [a], Michaela Wilhelm [a,*], Zhipeng Xie [b], Kurosch Rezwan [a,c]

[a] University of Bremen, Advanced Ceramics, Am Biologischen Garten 2, IW3, Germany
[b] State Key Laboratory of New Ceramics and Fine Processing, Department of Materials Science & Engineering, Tsinghua University, Beijing 100084, PR China
[c] MAPEX—Centre for Materials and Processes, University of Bremen, Am Fallturm 1, 28359 Bremen, Germany

HIGHLIGHTS

- Anisotropic macroporous SiOC monolith showed promising properties for cryogenic wicking.
- Unidirectional porous structures, allowed for preferential adjustment of physical properties in different directions.
- The compressive strength of monoliths in liquid nitrogen (77K) was found twice as high as that in air (293K).
- Pyrolysis temperature changed both mesoporosity and composition of monoliths and influenced compressive strength.
- Anisotropic coefficients of thermal expansion of porous monoliths agreed well with calculation from Schapery equation.

GRAPHICAL ABSTRACT
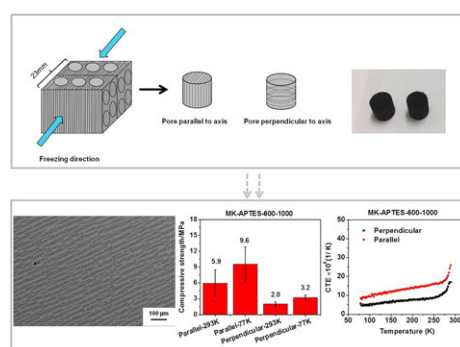
ABSTRACT

Macro/mesopore SiOC ceramic monoliths of anisotropic structure were prepared by freeze casting, using methy phenyl polysiloxane (H44) or methy polysiloxane (MK) and (3-aminopropyl)triethoxysilane (APTES) as precursors. Influence of pyrolysis and testing temperature on compressive strength was investigated. Monoliths pyrolyzed at 700 °C had the highest compressive strength both at 77 K (14.0 ± 4.3 MPa) and 293 K (7.7 ± 1.8 MPa), regardless of precursors. Compressive strength of monolith in parallel direction is around twice as much as perpendicular direction. Compressive strength of both monoliths in liquid nitrogen (77 K) was around twice of that in air (293 K) probably due to low temperature and liquid resistance. Anisotropic expansion was observed, and the shrinkage in parallel direction was almost twice of that in perpendicular direction, which can be verified by the Schapery equation. Monolith made from H44 showed a much higher coefficient of thermal expansion at 77 K than monolith made from MK and APTES, probably due to difference in composition and measurement condition. Thermal conductivities and specific heat capacities displayed an upward trend from low to warmer temperature. The minimum and maximum values for thermal conductivity are 0.2 and 1.2 W m^{-1} K^{-1}. The maximum heat conductivities might be determined mainly by the macroporosity and the thermal conductivity of the hybrid material.

* Corresponding author.
E-mail address: mwilhelm@uni-bremen.de (M. Wilhelm).

1. Introduction

Solid ceramics have attracted a lot of attention in cryogenic engineering; as supporting materials for superconducting magnet systems [1], as fuel cladding in nuclear power applications [2], and as bearings working in pressurized cryogenic fluids in space technology [3]. In the space industry, not only solid materials, but also porous structures have useful applications; porous materials have been used for phase separation and transport of storable and cryogenic fluids, such as liquid acquisition devices and propellant management devices. They enable a gas-free propellant delivery to the spacecraft's engines via capillary pressure driven flows in porous elements and bubble point pressure [4–6]. The delivery of cryogenic propellants in propellant management devices, in a system such as one that uses liquid O_2 as the oxidizer (boiling point 90 K) and liquid H_2 as the fuel (boiling point 20 K), etc. by capillary transport via porous medium, such as metallic weave, allows propellants to be transported without gravitational force in space. Zhang et al. investigated wicking (capillary rising) of liquid nitrogen into a porous metal weave in an open cryogenic chamber [7]. Grebenyuk et al. studied the wicking of liquid nitrogen into glass frits under isothermal conditions (77 K) [8]. Compared to metallic weaves, macroporous monolithic ceramics have a low density, high mechanical strength, and excellent corrosion resistance, making them potentially excellent mediums for cryo-wicking. Considering the wicking pumping capability and the wick permeability, the macropore size for this application should be around several to tens of micrometers [7–8]. Notably, the wicking behaviours of macroporous ceramics have also been studied for capillary-based heat pipes [9]. Different propellant liquids have different surface energy, thus adjustable surface characteristics of materials are preferred. The use of preceramic polymers as precursors for producing polymer-derived ceramics enables the adjustment of surface characteristics and the microporous structure [10].

Fabrication of macroporous ceramic monoliths using preceramic polymers faces numerous challenges for the wicking process, due to the relatively large monoliths required (several centimetres to tens of centimetres). A few methods are commonly used to produce macroporous ceramic monoliths: sacrificial templating, direct foaming, the replica method, and additive manufacturing [11]. The sacrificial template method results in samples with narrow pore size distributions, however, this method may be limited to membranes or small size sample to avoid severe shrinkage and cracking caused by template evacuation, which is particularly noticeable for large, bulky monoliths [12]. The direct foaming method normally results in samples with relatively wide pore size distributions and larger pores [13]. The freeze casting method, which is a special sacrificial templating method, is a good option for the fabrication of macropore monoliths with narrow pore size distributions [14].

The ceramics are fabricated at room temperature, but operate at cryogenic temperature. Additionally, they carry loads between ambient and low temperature components. Thus, it is very important to investigate the thermal and mechanical properties of the ceramics at cryogenic to room temperatures. There has been extensive investigation of mechanical properties of the ceramics at room temperature or higher temperatures, however, mainly on nonporous materials, like ceramic-matrix composites (CMC) [15], yttria-stabilized zirconia [16] or bioceramics [17]. For porous ceramics, mechanical property investigations have also been focused mainly on room or high temperature behavior. Seuba et al. investigated that honeycomb out-of-plane model derived by Gibson and Ashby can be applied to describe the compressive behavior of unidirectional porous yttria-stabilized zirconia prepared by freeze casting [18], in their work, maximum compressive strength of 286 MPa was achieved for sample with 49.9% porosity and pore size of 3 μm. Dey et al. investigated the porosity-dependent variation of fracture strength (9–34 MPa) and elastic modulus (7–28 GPa) of mullite-bonded porous SiC ceramics at room temperature [19]. The flexural strength (57 ± 6 MPa) and fracture toughness ($1.5 \pm 0.1 MPam^{1/2}$) of freeze-cast porous Si_3N_4 composites have also been investigated, and the mechanical properties can be improved with addition of polyacrylamide (PAM) [20]. Meille investigated the transition of elastic, brittle, and cellular behavior of porous ceramics when porosity (30%–75%) and pore size (hundreds microns to several microns) changed, maximum compressive strength 170 ± 68 MPa and minimum compressive strength of 9 ± 1.2 MPa [21] were found. Mechanical properties of silicon oxycarbide ceramic foams have also been investigated, compressive strength ranged from 1.31 ± 0.51 MPa (600 ± 145 μm) to 9.90 ± 1.78 (100 ± 40 μm) was obtained depending on the foam density, and longer exposure to 1200 °C led to the decrease of compressive strength [22].

Thermal properties of the crystalline and/or amorphous dense ceramics at cryogenic temperatures or higher have been examined. Normally the thermal conductivity of SiC is measured at 300 K. At this temperature single-crystalline SiC shows values in the range of 150 to 500 W m^{-1} K^{-1} depending on the purity, polymorph, etc. High pure crystalline SiC measured from 3 K to 300 K showed a nonlinear thermal conductivity of 6–5200 W m^{-1} K^{-1} and impurities decreased the conductivity greatly [23]. Thermal properties of ceramics for thermal barrier coatings have been reviewed by Cao et al., for example, at 1273 K thermal conductivities of ZrO_2, Mullite, and Al_2O_3 are 1.56, 3.0 and 1.7 W m^{-1} K^{-1} [24]. There are also work investigating thermal properties of porous ceramics at room or higher temperatures. Thermal conductivity of porous SiC (porosity ~ 70%) was observed to be ~2 W m^{-1} K^{-1} [25], a SiC foam with pore sizes between 0.4 and 2 mm showed 0.4–2.7 W m^{-1} K^{-1} [26] and porous nano-SiC showed 2 W m^{-1} K^{-1} at 300 K [27]. Ultra-low thermal conductivity 0.06 W m^{-1} K^{-1} was achieved for porous yttria-stabilized zirconia (porosity 52–76%, pore size 0.7–1.8 μm) fabricated by tert-butyl alcohol (TBA)-based gel-casting process [28]. Thermal conductivity of porous alumina (porosity 6–47%, pore size 5–50 μm) was investigated from room temperature to 500 °C and the temperature dependence of different porosity was fitted with second-order polynomials and 1/T-type relations [29]. The effective thermal conductivity of macroporous SiOC ceramics is 0.041 to 0.078 W m^{-1} K^{-1} at room temperature, depending on the density [30]. There has been some theoretical work investigating the thermal conductivity bounds for isotropic porous materials [31] and analytical relations describing effective thermal conductivities with pore volume fractions [32]. Most of the work has focused on investigating the thermal properties of isotropic porous ceramics. Pappacena et al. studied the thermal conductivity of biomorphic anisotropic silicon carbide at room and high temperatures [33]. However, little research has been performed on the thermal conductivity of anisotropic porous ceramics from cryogenic to room temperatures.

Our work intends to begin to fill this gap by investigating the thermal and mechanical properties of the anisotropic porous monoliths for cryogenic wicking. The derivation of porous ceramic monoliths of high permeability, low thermal conductivity and relatively high mechanical properties, provides a new horizon for porous materials for cryogenic applications, beginning with heat and mass transport.

2. Materials and methods

Macroporous ceramic monoliths were prepared by freeze casting, using hybrid fillers as the main solid phase. Two kinds of hybrid fillers were prepared, using different precursors: pure methyl phenyl polysiloxane (H44) and methyl polysiloxane (MK) together with (3-aminopropyl)triethoxysilane (APTES) by the following two different routes (A and B). These processes produced similar porous ceramics, however, different compositions. Two processes (Fig. 1) were chosen to investigate if the precursors and cross-linking will have an influence on the properties of final porous ceramics.
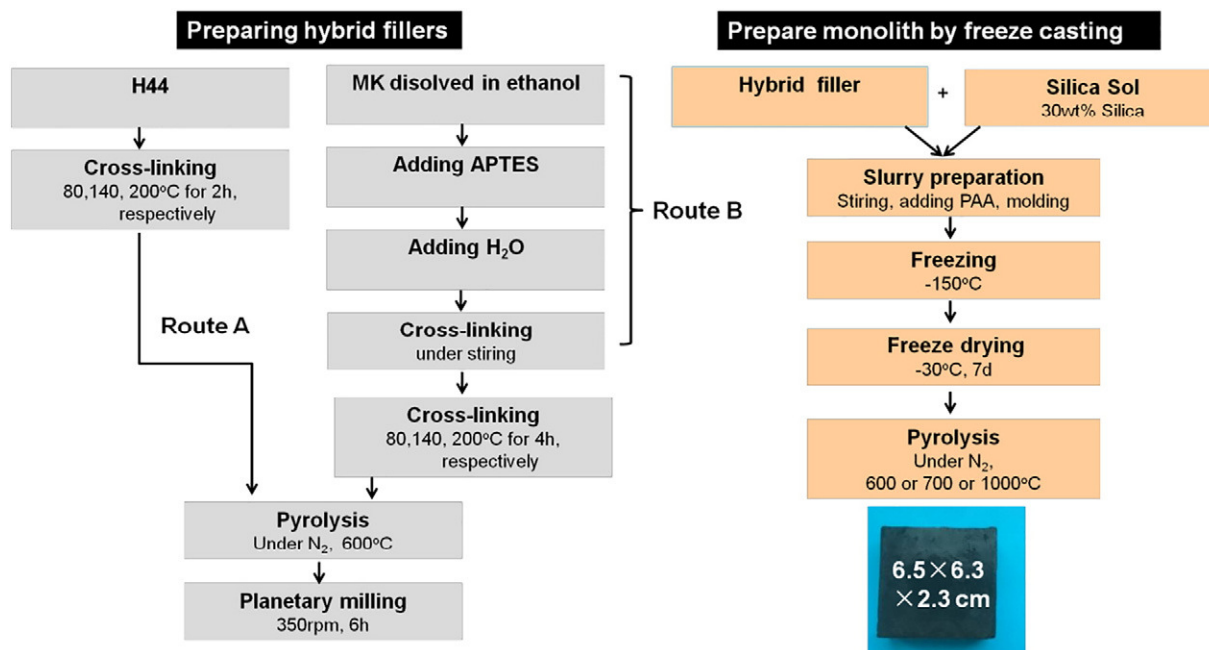
2

Fig. 1. Process scheme, parameter variations of synthesized samples and the monolithic structure of the resulting pyrolyzed sample.

2.1. Preparation of hybrid filler

2.1.1. Route A

H44 was pre-cross-linked using a multi-stage heat treatment in air at 353 K, 413 K, and 473 K (all dwell times 2 h), with a heating rate of 60 K h^{-1} between dwell times. The pre-cross-linked polysiloxane pieces were then pyrolyzed at 600 °C (873 K) under nitrogen atmosphere. The heating rate was set to 120 K h^{-1}, up to 500 °C (773 K), and then 30 K h^{-1} to the final temperature, with a dwell time of 4 h. These fillers were given the nomenclature "H44-600".

2.1.2. Route B

MK was first dissolved in ethanol, and then mixed with (3-aminopropyl)triethoxysilane (APTES) in a molar ratio of 1:1. Water is used to catalyze cross-linking. A solid was formed gradually and then transferred to a cross-linking oven using a multi-stage heat treatment in air, at 353 K, 413 K, and 473 K (all dwell times 4 h), with a heating rate of 60 K h^{-1} in between dwell times. The pre-cross-linked polysiloxane pieces were then pyrolyzed at 600 °C (873 K) under a nitrogen atmosphere. The pyrolysis conditions were the same as route A (above). These fillers followed the nomenclature "MK-APTES-600". More details about preparation can be found in previous literature [34].

Fillers obtained by both routes were ground by planetary ball milling at 350 r min^{-1} for 6 h to get fine powders. The particle sizes are mostly below 1 μm, [34] and due to the surface charges of the particles, particle separation by sieving was not possible. These powders were ready to be used in freeze casting steps.

2.2. Freeze casting process

30 wt% (weight percent) of precursor powders were added to 70 wt% of silica sol (with 30 wt% SiO_2 nanoparticles, 8 nm, BegoSol® K, BEGO) under stirring. The silica sol acted as a binder and water source during the freezing process. The pH was adjusted between 6 and 7, using polyacrylic acid (PAA, Sigma) to ensure that the condensation reaction of the silica sol proceeded to completion. The obtained slurry was then placed under vacuum at 300 mbar for 5 min to eliminate bubbles created during stirring. It was then poured into a mold, which comprised of two aluminum plates and a PVC U-shaped mold (see

Supplementary Fig. 1). This was quickly transferred to a deep freezer (−123 K) for half an hour. The samples were then dried in a freeze dryer for 7 days at 243 K. Finally, they were pyrolyzed at 600 °C (~873 K), 700 °C (~973 K) and 1000 °C (~1273 K) in an atmosphere of nitrogen. The monoliths were given the nomenclature "H44-600-xxx" and "MK-APTES-600-xxx", depending on the fillers used.

2.3. Characterizations

The solid (true density) densities of both monoliths were measured by Helium pycnometer (Accupyc 1330, Micromeritics, USA). The particle sizes and pore morphologies of samples were analyzed with scanning electron microscopy (SEM, field-emission SEM SUPRA 40, Zeiss, Germany) operating at 2.00 kV mounted on carbon tape. Samples were embedded in resin and polished and later sputtered with gold before measurements. Mercury intrusion porosimetry (Pascal 140/440, POROTEC GmbH, Germany) was used to determine macroporosities. Compression tests at 77 K and room temperature were performed on a universal testing machine (Zwick/Roell 2005, Zwick, Germany) universal testing machine, using cylinder monolith samples, at a constant displacement rate of 0.5 mm/min.

The samples were cut in two different directions and two types of cylinder monoliths (Diameter: 9.4–9.5 mm, height 9.4–9.5 mm) were obtained for compression tests; the first with lamellar pores parallel to the cylinder axis, and the second with pores perpendicular to cylinder axis. The compression tests were carried out in liquid nitrogen (77 K), ethanol-dry ice bath (195 K), pure ethanol bath (293 K) and in air (293 K). Ten specimens were tested for each experimental condition. For the compression test at low temperatures, the samples were dried at 343 K for 7 days. Prior to and during the test, the samples were immersed under the liquid nitrogen/ethanol-dry ice bath and liquid nitrogen/ethanol-dry ice was added continuously so that the monoliths were always fully submersed in the liquids to avoid the formation of ice in the pores before and during the loading and equilibrate inner temperature with the liquids. A steel half sphere made of (diameter: 12 mm) was placed on the top of the monolith in order to minimize the effects of superficial defects and misalignment during the compression test. Compressive strength was calculated based on maximum load at the end of the elastic stage.

The linear thermal expansions were measured using a strain gauge (Type: BB120-2AA-W250, Gauge Factor: 1.74 ± 1 %, Zhonghang Electronic Measuring Instruments Co., LTD, China) over a temperature range of 80-300 K. The fused silica was measured at the same time, and its corresponding linear thermal expansion data was used as a reference. Before the measurement, the samples were glued to the strain gauge using epoxy and pressed between 2 plates to ensure the full contact of sample and strain gauge. The sample with the strain gauge was then dried for 24 h. The sample with the strain gauge was put inside a closed measurement cell, cooled by liquid nitrogen inside a thermal insulator, and the thermal expansion was measured during the warming up of the sample.

Thermal conductivities were measured under the condition of steady-state longitudinal heat flow in vacuum from 77 K to 293 K. Steady-state method measured the heat flux through a length in the directional normal to a surface area; under a steady-state temperature difference (temperature difference does not change with time). In this work, rectangular shaped samples were used and two sides of the sample were glued by silver conductive adhesive to the two copper plates, acting as a heat source and a heat sink with known power output, which resulted in temperature drop across a given length and the temperatures at both sides were recorded. Both thermocouples and thermometers were used in this apparatus, and the details about the configuration and measurement can be found in the work of Liu et al. [35]. The steady-state technique used in this paper is an absolute technique, the sample was directly placed between a heat source and a heat sink, and therefore, no reference was used. The thermal conductivity was calculated by the software based on one-dimensional Fourier conduction equation $Q = -\lambda A dT/dx$, where Q is the heat flow rate, λ is the thermal conductivity, A is the cross-sectional area, and dT/dx is the temperature gradient. Low temperatures were achieved via compressed argon. Prior to the thermal conductivity measurement, the sample was glued to a measurement plate using a thin layer of silver conductive adhesive (adhesive viscosity was high, in order to avoid penetration into the porous sample), then dried overnight. Specific heat capacity was measured using differential scanning calorimetry (DSC, TA instruments) from 100 K to 293 K. Water vapour adsorption measurements were carried out by placing vessels with ~0.5 g of sample powder (particle sizes ≤300 μm) inside closed Erlenmeyer flasks filled with the solvents at equilibrium with their vapour phase at room temperature. Samples were weighed at the start and end of a 24 h measurement period in order to determine the vapour uptake of the material. The water content in the samples was investigated by thermogravimetric analysis (STA 503, Baehr), under a flow of nitrogen (2 L h^{-1}), using heating rates of 2 K min^{-1}.

3. Results

The polysilxoanes convert at 1000 °C completely from preceramic polymers to ceramics and the FTIR of the materials used in this work can be seen from the literature [36]. The compositions of SiOC materials prepared with different precursors are consisted of domains of SiO_2, and free carbon [37]. The solid density (independent of porosity) of H44-600-1000 is 2.0763 ± 0.0048 g cm^{-3}, and the solid density of MK-APTES-600-1000 is 2.3145 ± 0.0055 g cm^{-3}. The solid density of H44-600-1000 is lower than that of MK-APTES-600-1000; therefore, the free carbon content is higher in H44-600-1000.

The macroporosity of the monoliths prepared with two different fillers were measured by Hg-porosimetry, as shown in Fig. 2. The two monoliths have similar open porosities and pore size distributions; 58% and 20–50 μm for H44-600-1000, and 55% and 20–50 μm for MK-APTES-600-1000. The similarities in macroporosity are likely due to the same weights of solid loading and precursor particle sizes and freezing conditions. The slight differences in porosity and pore sizes might be due to solid volume differences of fillers, macrostructures changed slightly after pyrolysis.
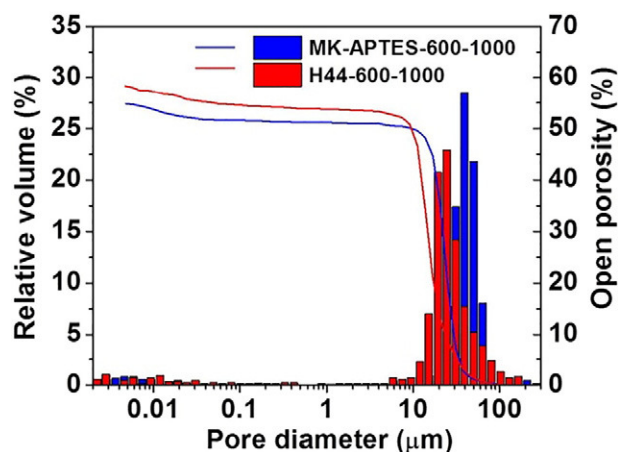

Fig. 2. Pore size distribution versus relative pore volume and open porosity curves obtained from Hg-porosimetry of pyrolyzed samples prepared with two different precursors.

Fig. 3 shows cross-sectional view of pores parallel to monolith axis. Both H44-600-1000 and MK-APTES-600-1000 show the similar structure. The geometry of the macroporosity is the negative replica of the ice crystals that formed during the freeze casting. Water crystallizes in the hexagonal crystal system, with the ice crystals having a growth velocity much faster in the a-direction of the hexagonal base than in the perpendicular c-direction. As a result, ice crystals develop a lamellar microstructure parallel to the a-direction, resulting in a lamellar spacing. The ice front propagation follows the temperature gradient, which was controlled by the configuration of the mold in this work. The SEM shows the unidirectional porous structure of the monolith. The lamellar pore size is defined as the distance between walls. Fig. 3a shows that the lamellae length can be up to several millimetres. Fig. 3–c illustrates that the distance between lamellar walls is around 30 μm, which agrees with the result of Hg intrusion porosimetry. Additionally, mesoporosity were observed in the samples, and were very similar for both samples, as shown in Supplementary Fig. 1.

During the freezing process, temperature gradients extended from the aluminum plates to the centre of the mold, as shown in Supplemental materials Fig. 2. This resulted in a monolith with unidirectional pores, however, a "stitching" structure would result in the very middle, as shown in Fig. 3d. This was observed when using double-sided freezing [38]. This stitching line is avoided during sample cutting for the compression test.

Additionally, the samples were placed under SEM before and after a 3-day liquid nitrogen immersion test; no obvious structural changes were observed (not shown in the article). Furthermore, no obvious crack propagation during the liquid nitrogen treatment could be observed. Both monoliths showed anisotropic compressive strength (Fig. 4), with "parallel" directions having the higher strength than the perpendicular directions. Compressive strengths were calculated to be 5.9 ± 2.5 MPa (parallel) and 2.0 ± 0.3 MPa (perpendicular) for MK-APTES-600-1000 and 4.3 ± 1.3 MPa (parallel) and 1.6 ± 0.9 MPa (perpendicular) for H44-600-1000 at 293 K. The parallel direction, with more continuous solid material, had higher strength.

Samples tested in liquid nitrogen (77 K) showed much higher compressive strength than those at 293 K (in air). Compressive strength in parallel direction improved from 4.3 to 9.6 MPa and from 5.9 to 9.6 MPa for H44-600-1000 and MK-APTES-600-1000, respectively. The compressive strength of MK-APTES-600-1000 is slightly higher than that of H44-600-1000.

Statistical tests (t-test) were conducted with the resulting data. The compressive strength for parallel directions at two different temperatures 77 K and 293 K are statistically different (p < 5%) for both MK-APTES-600-1000 and H44-600-1000. For the perpendicular directions,
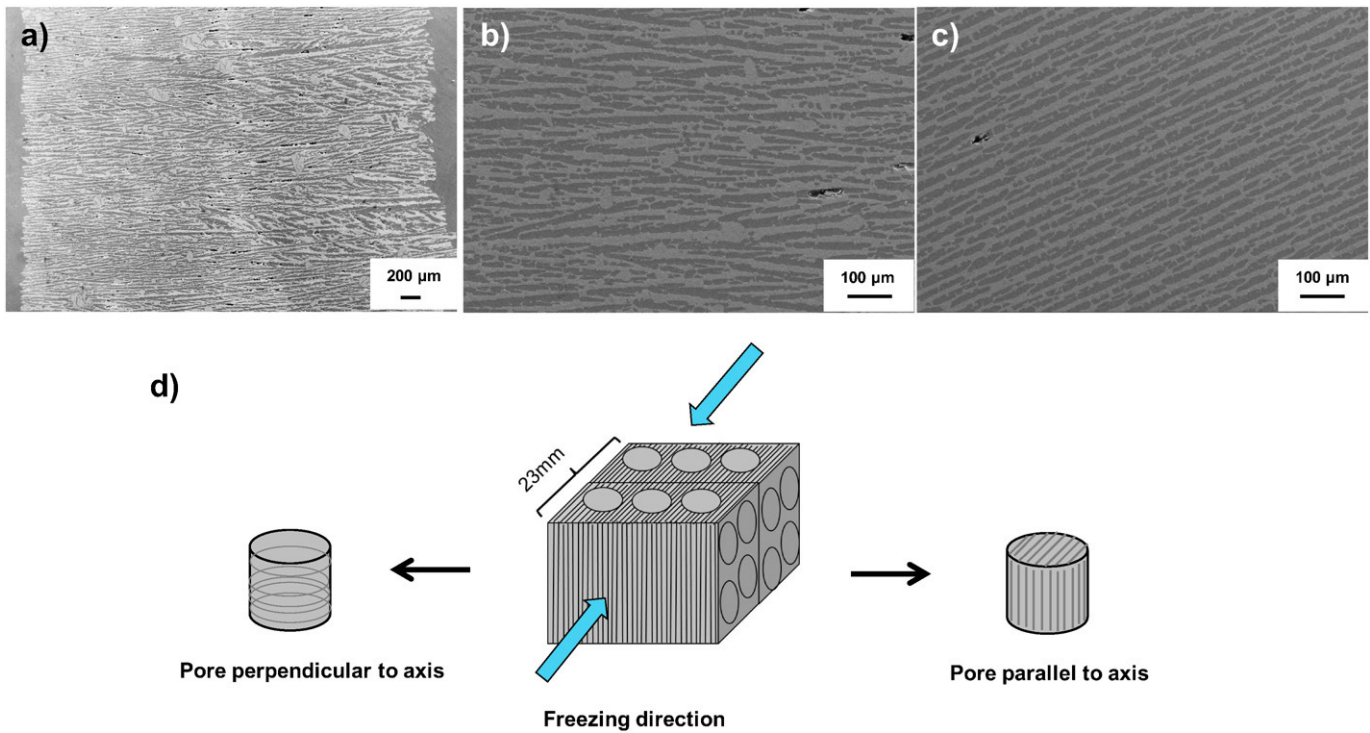
Fig. 3. SEM images of pyrolyzed monoliths. a–b) Cross section showing pores parallel to H44-600-1000 monolith axis, c) Cross section showing pores parallel to MK-APTES-600-1000 monolith axis, d) schematic of monoliths cut from different directions.

however, the compressive strengths are not statistically different due to the relatively low compressive strength and high standard deviation. The lamellar porous structure makes it not possible to distinguish the cracks paths from the lamellar pores. Therefore, it cannot be determined if the temperature influence the fracture modes.

The influence of the pyrolysis temperature on compressive strength was investigated by pyrolysis at 600, 700, and 1000 °C, as shown in Fig. 5. Anisotropic compressive strength was observed for all samples and compressive strength was influenced by pyrolysis temperature.

Overall, samples pyrolyzed at 700 °C show higher compressive strengths than samples pyrolyzed at 600 °C and 1000 °C at both 77 K and 293 K. The compressive strength of MK-APTES-600-xxx monoliths (parallel) pyrolyzed at 600, 700, and 1000 °C were 5.94, 7.71, and 3.42 MPa at 293 K and 9.57, 13.96, and 6.90 MPa at 77 K, respectively. Pyrolysis temperature influenced not only the final composition, but also the porous structure of the ceramics.

Samples pyrolyzed at 600 °C were weaker due to the considerably higher numbers of mesopores compared to samples pyrolyzed at 700

and 1000 °C [34]. The lower compressive strengths of samples pyrolyzed at 1000 °C compared to those pyrolyzed at 700 °C might be ascribed to the lower fracture toughness of MK-APTES-600-1000, which is strongly related to the composition of the samples. The lower fracture toughness of ceramics led to monoliths being more sensitive to crack propagation during loading in the compression test, which resulted in lower compressive strength [39]. However, the toughness was not measured in this work.

The linear thermal expansions of the monoliths were investigated from 80 K to 293 K during the warming up of the sample, which were shown in Fig. 6. Lattice contracted with decreasing temperature, which is typical for materials with positive coefficients of thermal expansion. The smooth plots indicated no phase transformations during the temperature variation and no detachment of strain gauge from sample surface. Both monoliths showed anisotropic coefficients of thermal expansion (CTE), and CTE in parallel direction is twice as that in perpendicular direction. The overall shrinkage of the MK-APTES-600-1000 at around 80 K versus room temperature were 1.7 and 2.9‰, as well as
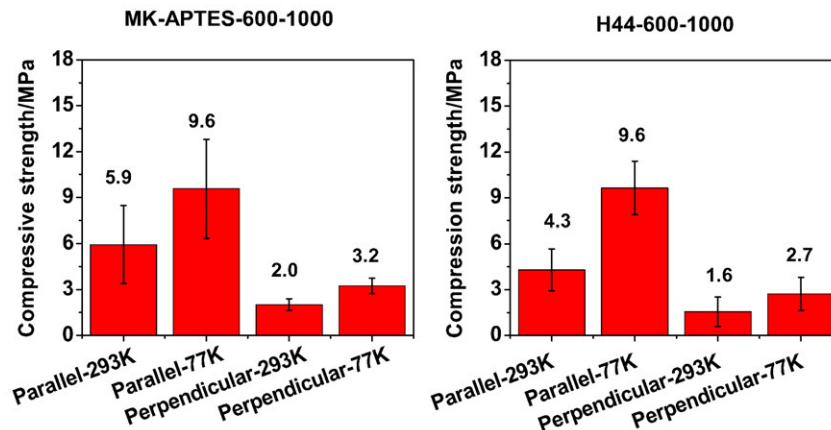

Fig. 4. Compressive strength of monoliths pyrolyzed at 1000 °C, at 77 K inside liquid nitrogen and at room temperature in air.
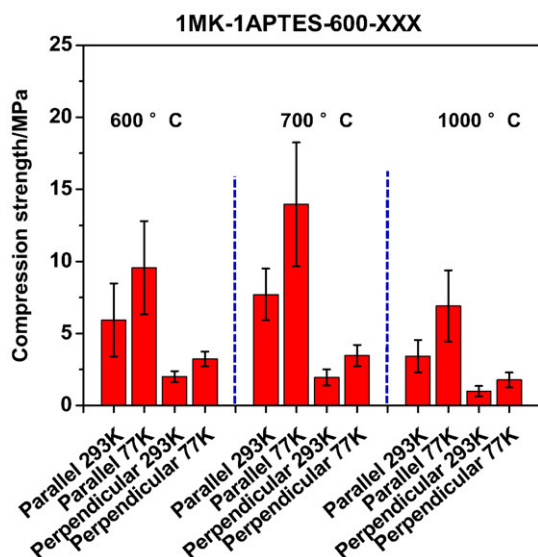
Fig. 5. Compressive strength of the MK-APTES-600-xxx samples, pyrolyzed at 600, 700, and 1000 °C, tested at 77 K in liquid nitrogen and at 293 K in air.

2.75 and 4.5‰ for H44-600-1000 in perpendicular and parallel directions, respectively.

The thermal expansion coefficients increased gradually with temperature from 80 K up to 250 K. From 250 K to 290 K, however, the measured CTEs increased substantially may be due to the large error introduced by the temperature drift of the sensor. The CTEs of MK-APTES-600-1000 increased from 4.5×10^{-6} to 8.7×10^{-6} K^{-1} (perpendicular) and 8.0×10^{-6} to 16.0×10^{-6} K^{-1} (parallel) in the temperature range of 80–250 K, while CTEs of H44-600-1000 increased from 7.0×10^{-6} to 14.6×10^{-6} K^{-1} (perpendicular) and 11.6×10^{-6} to

24.1×10^{-6} K^{-1} (parallel) in the temperature range of 80–250 K. It is worth mentioning that the thermal shrinkage of the H44-600-1000 samples was around twice as much as MK-APTES-600-1000.

The thermal conductivity of the monoliths was measured with steady-state longitudinal heat flow from 77 K to room temperature (Fig. 7). Anisotropic thermal conductivity was observed for both monoliths prepared with different fillers. With increasing temperature, thermal conductivity increased, analogous to similar amorphous materials, for which thermal conductivity is several orders of magnitude smaller than those of crystalline materials [40]. The minimum and maximum values for thermal conductivity are 0.2 and 1.2 W m^{-1} K^{-1}; comparable to nonporous SiOC ceramics (from 153 K to 1200 K) [41]. The specific heat capacities of the samples were also investigated. Despite greatly differing compositions, the samples showed very similar Cp values: around 0.319 J g^{-1} K^{-1} at 100 K to 0.740 J g^{-1} K^{-1} at room temperature for H44-600-1000, and 0.271 J g^{-1} K^{-1} at 100 K to 0.718 J g^{-1} K^{-1} at room temperature for MK-APTES 600-1000-DSC. Specific heat capacity of MK-APTES-600-1000 increased with increasing temperature linearly from 100 K to room temperature. However, a little abnormality was observed for H44-600-1000 from 90 to 160 K, which cannot be explained so far.

Lastly, permeability along the monolith axis (parallel) was measured with a modified falling head permeability test using water as the medium, and compressed air to vary the pressure (see Supplementary Fig. 3); this testing showed a permeability of 3.5×10^{-9} m^2. The high permeability is ascribed to the open porosity of the unidirectional channels.

4. Discussion

4.1. The influence of environmental temperature on compressive strength

Some studies have shown that mechanical properties of solid ceramics improve at cryogenic temperatures. Zirconia-based ceramics
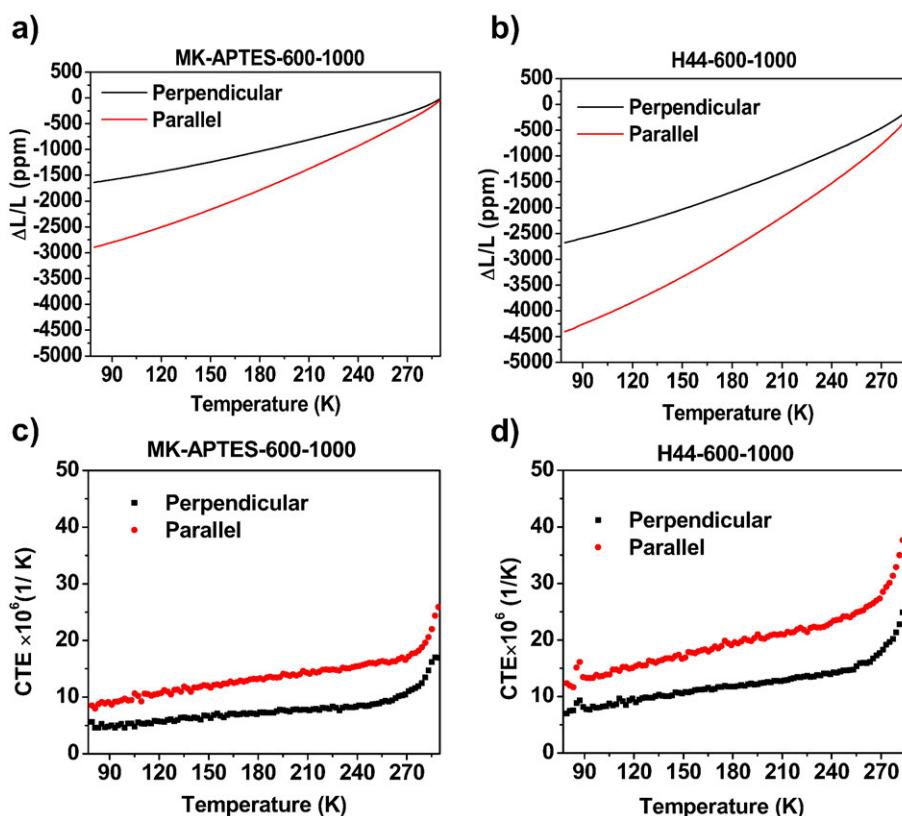

Fig. 6. a–b) Linear thermal expansion and c–d) coefficient of thermal expansion (CET) of pyrolyzed monolith in two directions.
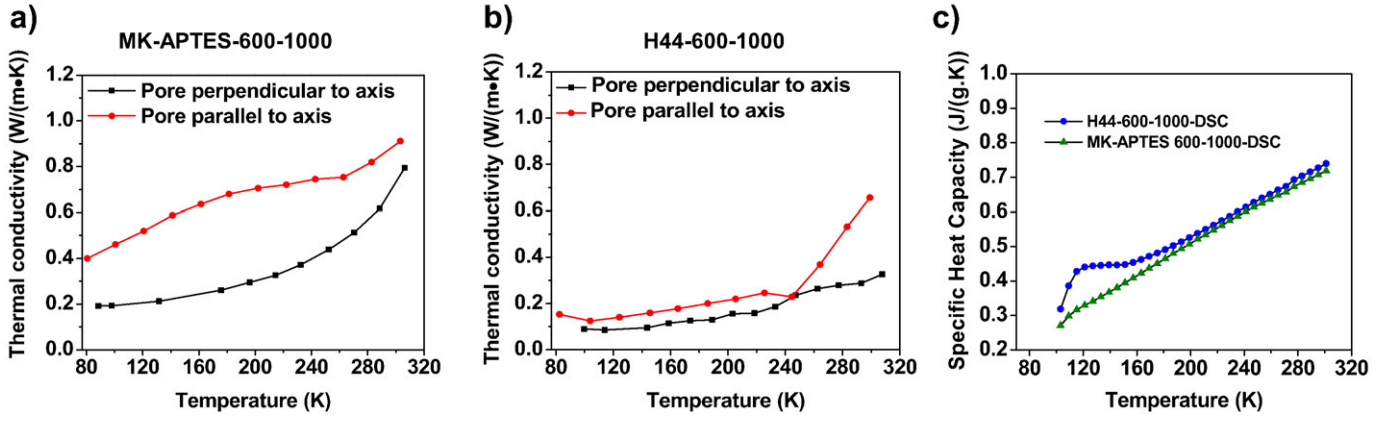
6

Fig. 7. a–b) Thermal conductivity of the pyrolyzed ceramic monoliths from 77 K to room temperature using steady-state longitudinal heat flow, c) Specific heat capacity of two pyrolyzed ceramic monoliths, measured by DSC from 100 K to room temperature.

have enhanced transformation toughening after cryogenic treatments, due to temperature-induced phase transformations [42]. Improved fracture strengths of reaction-bonded SiC composites [43] as well as Si_3N_4-SiC ceramics [44] were found at 77 K compared to that at 293 K, due to decreases in the cracks' effective size and increases in propagation resistance or more crack deflection (along crack propagation paths) at cryogenic temperatures. However, little work exists on the mechanical properties of amorphous porous ceramics, which involves no phase transformations.

For porous ceramics, compressive strength is normally influenced by the architecture, porosity, pore size, wall thickness, ceramic bridges between lamellae, and the testing conditions—like loading speed or sample size. Compared to solid ceramics, when temperature is decreased, the distance between the atoms get smaller, and, accordingly, the pore size at all scales should decrease. The prepared SiOC ceramics have a hierarchically-ordered porous structure, including macropores, mesopores, and micropores (600 °C and 700 °C) [34]. The most significant structural influence on the compressive strength comes from the macropores, as they're the largest defects.

One possible explanation for the improvements in the compressive strength of these samples may be the shorter interatomic distances at lower temperatures. It has been reported that compressive strength becomes stronger due to the lattice parameter change at cryogenic temperature [45]. This effect has been observed specifically for bulk metallic glasses $Zr_{41.25}Ti_{13.75}Ni_{10}Cu_{12.5}Be_{22.5}$ at cryogenic temperatures, which also led to strength improvements [46]. In ceramics, the grain boundaries and the pores (cracks) can decrease the strength greatly. A fracture begins with crack nucleation and then propagates. The influence of crack size on the strength can be seen from Griffith equation:

$$\sigma_{Griffith} = \sqrt{\frac{2\gamma_0 E}{kl}}$$

where l is the crack size, γ_0 is the surface energy, E is the elastic modulus, and k is a dimensionless term related to crack and sample geometry. The shorter atom distances result in weaker atomic vibration and stronger interatomic interaction. Accordingly, the elastic modulus and surface energy increase. All those factors lead to the strength increase.

Another reason for the strength improvement might be the liquid nitrogen entrapped in the pores. The compression test at 77 K was achieved by placing the samples directly into the liquid nitrogen. The liquid nitrogen entered the pores, due to the high permeability. During the compression test, the samples were immersed in liquid nitrogen, to keep the temperature equilibrium and to exclude moisture getting into the porous structure. Due to the little compressibility of both liquid and solid, the liquid cannot be squeezed out, and it was trapped inside the porous structure. Therefore, the porosity was 'lowered' due to the

trapped liquid inside the structure, which led to the increased compressive strength. In order to investigate the influence of liquids on compressive strength, 'parallel' 1MK-1APTES-600-1000 was tested in ethanol-dry ice bath (195 K) and pure ethanol (293 K). The results are shown in Supplementary Fig. 4. The compressive strength at 195 K was higher than when tested at 77 K. The higher viscosity of ethanol compared with liquid nitrogen may be responsible for the difference. Compressive strength in pure ethanol (293 K) was much higher than tested in air (293 K). Thus, it can be surmised that the major improvements in compressive strength in liquid nitrogen were due to the liquid as well as the cryogenic temperature.

Due to the capillary effect provided by the porous structure, in addition to the relatively hydrophilic ceramic surface, water in the air condenses easily on the inner surfaces of the pores. At cryogenic temperatures, these adsorbed water molecules may form ice grains inside the pores. The water vapour adsorption at room temperature, as well as the total cumulative volume determined from Hg intrusion porosimetry was used to evaluate possible water contents inside porous monoliths.

Taking the pore volume as measured by Hg intrusion as V_p, the water adsorption per gram of ceramics as W_{vapor}, the sample weight as m_s and the density of water as ρ, the volume of water adsorbed on the surface V_{water} may be calculated as:

$$V_{water} = \frac{W_{vapor} \times m_s}{\rho}$$

The volume percentage of water in the pores under saturated water vapour P_{water}, was calculated based on the following equation:

$$P_{water} = \frac{V_{water}}{V_p}$$

P_{water} was calculated to be 12 vol% and 11.6 vol% for H44-600-1000 and MK-APTES-600-1000 respectively (vol%: volume percentage). The water content in the air is much lower than the saturated atmosphere and samples were fully dried before being immersed into liquid nitrogen. Thermogravimetric analysis (see Supplementary Fig. 5) showed that the water adsorption is around 2.0%wt; this increased to around 5.7%wt after storing in air for one day. This can be viewed as the phase equilibrium of vapour and liquid water inside the capillaries. This shows that the volume of water in the pores was quite low, and the influence it may have had on the compressive strength of the monoliths was slight. In order to completely exclude the possibility of ice formation inside the porous material via atmospheric water vapour, further compression testing at cryogenic temperatures will need to be carried out in a protective atmosphere.

4.2. Influence of compositions and anisotropy on coefficients of thermal expansion

The CTE of the H44-600-1000 sample was around twice as much as MK-APTES-600-1000. The composition difference between two monoliths contributed to the difference in thermal expansion. The solid density of H44-600-1000 is lower than that of MK-APTES-600-1000; therefore, free carbon content is higher in H44-600-1000. There have been reports using the composition to alter the CTEs [47–48]. Free carbon (forming turbostratic graphite domains) has generally higher thermal expansion than amorphous silica. Amorphous silica has a CTE lower than 1.0×10^{-6} K^{-1} CTEs [49], however, amorphous carbon has a CTE of 1.5–7.0×10^{-6} K^{-1} [50]. Besides composition difference, the measurement condition should be also responsible for the observed difference in the CTEs of the two monoliths. In contrast to CTEs of solid materials, the measurement conditions of porous materials need to be specified. There are two extreme conditions: undrained condition or drained condition [51]. Drained condition corresponds to the behavior of dry porous materials or the case of slow heating of a porous material in a way that the excess pore pressure can be entirely dissipated, therefore, the pore pressure is constant, whereas in undrained condition, the mass of the fluid phase is constant, and the fluid in pore volume generates an excess pore pressure, therefore thermal expansion increases. The measured CTEs of porous SiOC were higher than CTEs of solid SiOC in the literature, around 3.1×10^{-6} K^{-1}, which were measured at elevated temperature [52–53]. The measured CTEs of porous SiOC at cryogenic temperature can also be influenced by the. During measurement, samples were put inside a small closed, however, unvacuumed cell, therefore, the moisture which were previously present in the container, may condense in the samples during cooling. Considering that the surface characteristics of both materials are both hydrophilic, they might also contain a certain amount of water even after drying. Due to the small size of the cell and the fact that samples were covered by the strain gauge with glue, the large amounts of moisture from air should be excluded, so the measurement condition can be considered to be between undrained condition and drained condition. The plots $\Delta L / L$ in Fig. 6 are very smooth without abrupt change, which means that there is no obvious phase transformation (ice to water). This excluded great amounts of moisture inside the porous structure. However, the measurement condition may be responsible for relatively high CTEs of porous SiOC at cryogenic temperature.

The SiOC ceramic monoliths have anisotropic macroporous lamellar pores (porosity of 58% and 55%) and mesopores. Both macropores and mesopores should have no influence on the coefficients of thermal expansion [54–55]. Large and open pores play no role in the accommodation of thermal expansion, whereas the closed pores (transcrystalline cleavage cracks or microcracks created during temperature change) can accommodate thermal expansion [56], often result in anomalous thermal expansion, like negative and zero thermal expansion coefficients [57]. During cooling to cryogenic temperature, there were no macroscopic cracks observed in SiOC samples, however, microcracks cannot be determined due to the lamellar porous structure.

Lamellar porous SiOC monolith can be considered as 'composite' made of aligned solid walls and lamellar pores filled with air. There has been work, predicting the coefficients of thermal expansion α_c of fiber reinforced ceramics [58] or composite materials [59] prepared by freeze-casting and infiltration by using the models proposed by Kerner [60] and Schapery [61]. According to Schapery equation, CTEs in the longitudinal direction (parallel) α_l and transverse direction (perpendicular) α_t are as following:

$$\alpha_l = \frac{E_p \alpha_p V_p + E_s \alpha_s V_s}{E_p V_p + E_s V_s}$$

$$\alpha_t = (1 + v_p)\alpha_p V_P + (1 + v_m)\alpha_s V_s - \alpha_l(v_p V_P + v_s V_s)$$

where E is the elastic modulus, V is the volume fraction, and α is the coefficient of thermal expansion, ν is the Poisson's ratio. The subscript s and p denote solid and pore (air). In case of porous materials, E_p, v_p, α_p are zero, therefore $\alpha_l = \alpha_s$, and $\alpha_t = \alpha_s V_s$. These results mean that the CTEs in parallel direction should not change with the porosity, which can also be seen from the work of Nakajima [62], whereas the CTEs in perpendicular direction will be influenced by the porosity. The porosity of 1MK-1APTES-600-1000 and H44-600-1000 is 55% and 58%, therefore, the solid volume V_s is 45% and 42%. The CTEs α_t is around half the value of α_l, which fits the theory very well.

4.3. Thermal conductivity of hierarchically-ordered porous monolith

The thermal conductivity of crystalline materials at lower temperatures rises before decreasing. The thermal conductivity of amorphous materials, however, increases with increasing temperature over this range, and is several orders of magnitude smaller than that of crystalline materials [63]. Impurities of less conductive materials, e.g. SiO$_2$, lower the overall conductivity of noncrystalline SiC material [23,64]. Porosity also considerably lowers thermal conductivity; however, it is less significant than bulk crystallinity [27]. Thermal conductivity in porous materials is comprised of solid contribution (main contribution), gas contribution (significantly smaller comparing with solid), radiative contribution (negligible at low temperature), convection contribution (pores smaller than 3–4 mm, is negligible) [33].

Both monoliths have a hierarchically-ordered pore structure, with mesopores inside the lamellar walls. To understand the relationship between the thermal properties and the microstructure, the structure was simplified to a 2-phase mixture (gas-solid composition), as shown in Fig. 8. The porous structure can be seen as layers of the solid separated
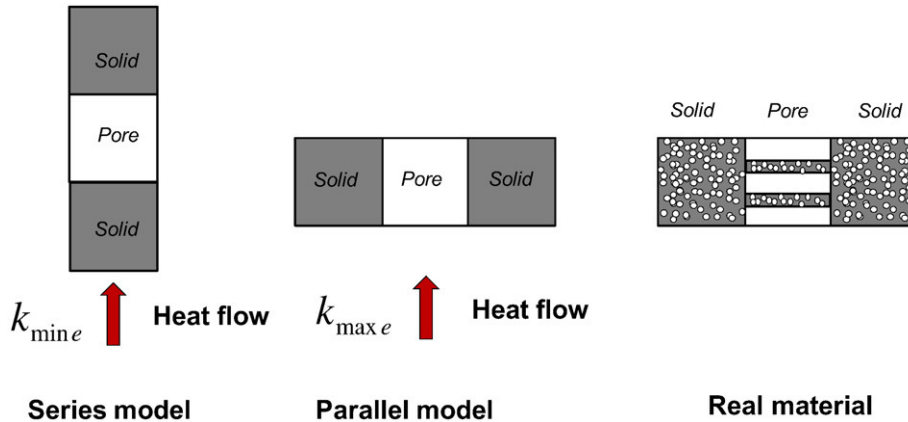

Fig. 8. Parallel and series models and simplified structure of the real material. Walls contain mesopores (white spheres).

by layers of air of uniform thickness, and the walls themselves had mesopores.

According to 'series' and 'parallel' models of thermal conductivity in a biphase, minimum effective thermal conductivity occurs in the series model, wherein the solid and the gas phases are in layers normal to the direction of heat flow. The maximum value of effective thermal conductivity occurs when the solid and gas phases are in layers parallel to the direction of heat flow, that is, the parallel model [65].

$$k_{\text{min}e} = \frac{k_{s-\text{wall}}k_g}{pk_{s-\text{wall}} + (1-p)k_g}$$

$$k_{\text{max}e} = pk_g + (1-p)k_{s-\text{wall}}$$

where $k_{\text{min}e}$ and $k_{\text{max}e}$ are the minimum and maximum effective thermal conductivity, p represents the macroporosity, $k_{s-\text{wall}}$ and k_g denote the thermal conductivity of the lamellar walls and the gas, respectively. If the 'gas' phase is a vacuum, k_g is 0. The lower boundary $k_{\text{min}e}$ and upper boundary $k_{\text{max}e}$ were calculated to be 0 and $k_{\text{max}e} = (1-p)k_{s-\text{wall}}$, respectively. However, this cannot be directly applied to the investigated freeze cast materials. Since in the freeze casted materials, the lamellae walls have bridges between each other as shown in Fig. 3, the bridges should be considered, shown in Fig. 8. A geometry factor C (at certain temperature range, C can be regarded as independent of temperature) is introduced. Then the k_g can be rewritten as $k_g = Ck_{s-\text{wall}}$. SiOC monolith was composed of nanodomains of SiO_2 and carbon, which is a hybrid material, and there are mesopores on the lamellar walls. The mesopores, can be considered spherical pores, a randomly interconnected skeleton, forming a two-phase "gas-solid composite" system. The effective thermal conductivity of the walls fits the assumption of the effective medium theory (EMT) model [66–67].

The EMT model $k_{s-\text{wall}} = \frac{1}{4}\{(3v_{meso-p}-1)k_g' + (3v_{solid}-1)k_{s-\text{hybrid}}$
$+[((3v_{meso-p}-1)k_g' + (3v_{solid}-1)k_{s-\text{hybrid}})^2 + 8k_g'k_{s-\text{hybrid}}]^{\frac{1}{2}}\}$ can be simplified to: $k_{s-\text{wall}} = \frac{1}{2}(3v_{solid}-1)k_{s-\text{hybrid}}$ when the measurement having been conducted under vacuum, v_{meso-p}, k_g' $(k_g' = 0)$ and $k_{s-\text{hybrid}}$ represent the mesoporosity inside the walls and the thermal conductivity of the air and hybrid materials. v_{meso-p} is very small at 1000 °C pyrolysis, pushing $k_{s-\text{wall}}$ very close to $k_{s-\text{hybrid}}$. The small influence of microscale spherical pores on the thermal conductivity at low temperatures (produced by gas emission during thermal decomposition) has also been reported by the Russell [68]. Therefore, $k_{\text{max}e} \approx (1-p)k_{s-\text{hybrid}}$; the maximum heat conductivity was determined mainly by the macroporosity and the thermal conductivity of the hybrid material. Since thermal conductivities of amorphous materials increase with temperature, it makes sense that the measured effective conductivities also increased with temperature. As discussed before, the solid phase contained nanodomains of carbon and silica, and the mesopores are on the lamellae walls. When the fractions of silica and carbon nanodomains are known, the thermal conductivity of the hybrid solid can also be calculated, based on the effective medium theory (EMT) model which has two solid-solid phases. However, the volume of carbon and silica in the hybrid is not known. Therefore, the thermal conductivity cannot be confirmed quantitatively. Thermal conductivity anisotropy decreases with increased solid loading, due to more bridges formed between lamellae. In this case, the bridge amounts are very similar for samples with both precursors [69].

4.4. Potential applications

The delivery of cryogenic propellants in propellant management devices are mainly governed by the behavior of cryogenic media in porous materials (cryo-wicking). The cryo-wicking is mainly influenced by the liquid properties in terms of density, surface energy, specific heat capacity, thermal conductivity, and the properties of the porous materials, such as density, specific heat capacity, thermal conductivity, porous structure, pore size and permeability, as well as the environmental conditions such as temperature of porous solid and cryogenic medial [8]. Due to the very low surface energy of liquid nitrogen (8.5 mN m^{-1}), the pore sizes for wicking should be within micrometer range. The pore size range (20–50 μm), low thermal conductivity (0.2 and 1.2 W m^{-1} K^{-1}) and high permeability (3.5×10^{-9} m^2) of these porous materials render the materials used in cryogenic liquid transport. The wicking behavior of monolith with radial porous structure prepared by this method under isothermal condition at 293 K has been investigation [70]. Materials for wicking experiments or other space applications need to survive a series of critical treatments before testing, such as sunisoidal vibration, random vibration, ultrasonic bath treatment, and high vacuum environment for long term. However, some particles were observed detached from the monoliths of this work after treatments. Therefore the mechanical strength should be further improved to enable practical cryogenic applications. One possible way is to convert SiOC ceramic monolith to SiC ceramic monolith at higher pyrolysis temperature to diminish mesopores and increase the bonding strength. However, by this the thermal conductivity will be improved as well, which may cause easier heat leak. Therefore, further investigation on how to improve mechanical strength should be done. Besides, the large capillary pumping capacity (small pore size, high permeability), also render these materials open as wicks such as loop heat pipe for cooling electronic components [71].

5. Conclusion

Porous SiOC ceramics prepared with different polysiloxanes by different cross-linking processes showed that they have slight differences in mechanical and thermal properties. The thermal properties (thermal conductivity, specific heat capacity) and mechanical properties were mainly influenced by the amorphous nature and macroporous structure. For certain cryogenic applications, the anisotropic thermal and mechanical properties in parallel and perpendicular directions, which were shown by the anisotropic porous SiOC monoliths, are desired. The very low thermal conductivities and relatively high compressive strength are very promising for use in cryogenic engineering. The linear thermal expansion of both materials showed anisotropy, and different CTEs for the two monoliths might be due to different compositions and measurement conditions. Liquid entrapped inside the porous structure and cryogenic temperature might both improve the compressive strength of porous monolith. The unidirectional structure resulted in a high permeability, facilitating a high liquid pumping ability, which is not only suitable for fluid mass transport at cryogenic temperatures, but also similar applications at higher temperatures.

about potential materials for capillary transport of cryogenic liquids. The authors thank Dr. Thomas Schumacher (University of Bremen), for helping design cryogenic container for compression test and Dr. Evgeny Pogorelov (University of Bremen), for his helpful comments about permeability measurements and thermal properties. The authors thank Harrison Reid (University of Bremen) for language proof reading.

Appendix A. Supplementary data

Supplementary data to this article can be found online at http://dx.doi.org/10.1016/j.matdes.2017.08.039.

References

[1] L.F. Li, Y.Y. Li, O. Sbaizero, S. Meriani, et al., J. Am. Ceram. Soc. 80 (4) (1997) 1005–1008.
[2] E. Rohmer, E. Martin, Christophe Lorrette, Mechanical properties of SiC/SiC braided tubes for fuel cladding, J. Nucl. Mater. 453 (2014) 16–21.
[3] R. Khanna, B. Basu, Sliding wear properties of elf-mated yttria-stabilized tetragonal zirconia ceramics in cryogenic environment, J. Am. Ceram. Soc. 90 (8) (2007) 2525–2534.
[4] D.E. Jaekle, Propellant Management Device Conceptual Design and Analysis: Galleries, AIAA-97-2811, 1997.
[5] M. Wollen, F. Merino, J. Schuster, C. Newton, Cryogenic Propellant Management Device: Conceptual Design Study, NASA/CR-010-216777, 2010.
[6] D.J. Chato, M.T. Kudlac, Screen Channel Liquid Acquisition Devices for Cryogenic Propellants, AIAA-2002-3983, 2002.
[7] T. Zhang, P. de Bock, E.W. Stautner, T. Deng, C. Immer, Demonstration of liquid nitrogen wicking using a multi-layer metallic wire cloth laminate, Cryogenics 52 (2012) 301–305.
[8] Y. Grebenyuk, M.E. Dreyer, Wicking of liquid nitrogen into superheated porous structures, Cryogenics 78 (2016) 27–39.
[9] B. Seidenberg, T. D. Swanson, Ceramic heat pipe wick, US 4883116 A.
[10] T. Prenzel, M. Wilhelm, K. Rezwan, Pyrolyzed polysiloxane membranes with tailorable hydrophobicity, porosity and high specific surface area, Microporous Mesoporous Mater. 169 (2013) 160–167.
[11] E.C. Hammel, O.L.R. Ighodaro, O.I. Okoli, Processing and properties of advanced porous ceramics: an application based review, Ceram. Int. 40 (2014) 15351–15370.
[12] P. Colombo, E. Bernardo, Macro- and micro-cellular porous ceramics from preceramic polymers, Compos. Sci. Technol. 63 (2003) 2353–2359.
[13] P. Colombo, M. Modesti, Silicon oxycarbide ceramic foams from a preceramic polymer, J. Am. Ceram. Soc. 82 (3) (1999) 573–578.
[14] H.X. Zhang, P.D. Nunes, M. Wilhelm, K. Rezwan, Hierarchically ordered micro/meso/macroporous polymer-derived ceramic monoliths fabricated by freeze-casting, J. Eur. Ceram. Soc. 36 (2016) 51–58.
[15] E. Volkmann, K. Tushtev, D. Koch, C. Wilhelmi, J. Göring, K. Rezwan, Assessment of three oxide/oxide ceramic matrix composites: mechanical performance and effects of heat treatments, Compos. Part A 68 (2015) 19–28.
[16] X.R. Ren, W. Pan, Mechanical properties of high-temperature-degraded yttria-stabilized zirconia, Acta Mater. 69 (2014) 397–406.
[17] Q.Z. Chen, J.L. Xu, L.G. Yu, X.Y. Fang, K.A. Khor, Spark plasma sintering of sol–gel derived 45S5 Bioglass®-ceramics: mechanical properties and biocompatibility evaluation, Mater. Sci. Eng. C 32 (2012) 494–502.
[18] J. Seuba, S. Deville, C. Guizard, A.J. Stevenson, Mechanical properties and failure behavior of unidirectional porous ceramics, Sci. Rep. 6 (24326) (2016) 1–11.
[19] A. Dey, N. Kayal, O. Chakrabarti, R.F. Caldato, M.D. de Mello Innocentini, V.G. Guerra, Investigations on material and mechanical properties, air-permeation behaviour and filtration performance of mullite-bonded porous SiC ceramics, Int. J. Appl. Ceram. Technol. 11 (5) (2014) 804–816.
[20] F. Ye, J.Y. Zhang, H.J. Zhang, L.M. Liu, Pore structure and mechanical properties in freeze cast porous Si_3N_4 composites using polyacrylamide as an addition agent, J. Alloys Compd. 506 (2010) 423–427.
[21] S. Meille, M. Lombardi, J. Chevalier, L. Montanaro, Mechanical properties of porous ceramics in compression: on the transition between elastic, brittle, and cellular behaviour, J. Eur. Ceram. Soc. 32 (2012) 3959–3967.
[22] P. Colombo, J.R. Hellmann, D.L. Shelleman, Mechanical properties of silicon oxycarbide ceramic foams, J. Am. Ceram. Soc. 84 (10) (2001) 2245–2251.
[23] G.A. Slack, Thermal conductivity of pure and impure silicon, silicon carbide, and diamond, J. Appl. Phys. 35 (12) (1964) 3460–3466.
[24] X.Q. Cao, R. Vassen, D. Stoever, Ceramic materials for thermal barrier coatings, J. Eur. Ceram. Soc. 24 (2004) 1–10.
[25] J.H. Eom, Y.W. Kim, I.H. Song, H.D. Kim, Processing and properties of polysiloxane-derived porous silicon carbide ceramics using hollow microspheres as templates, J. Eur. Ceram. Soc. 28 (5) (2008) 1029–1035.
[26] T. Fend, B. Hoffschmidt, R. Pitz-Paal, O. Reutter, P. Rietbrock, Porous materials as open volumetric solar receivers: experimental determination of thermophysical and heat transfer properties, Energy 29 (5–6) (2004) 823–833.
[27] P. Wan, Z. Wu, H. Zhang, L.Y. Gao, J.Y. Wang, Porous nano-SiC as thermal insulator: wisdom on balancing thermal stability, high strength and low thermal conductivity, Mater. Res. Lett. 4 (2) (2016) 104–111.

[28] L.F. Hu, C.A. Wang, Y. Huang, Porous yttria-stabilized zirconia ceramics with ultra-low thermal conductivity, J. Mater. Sci. 45 (12) (2010) 3242–3246.
[29] Z. Zivcová, E. Gregorová, W. Pabst, D.S. Smith, A. Michot, C. Poulier, Thermal conductivity of porous alumina ceramics prepared using starch as a pore-forming agent, J. Eur. Ceram. Soc. 29 (2009) 347–353.
[30] L. Qiu, Y.M. Li, X.H. Zheng, J. Zhu, D.W. Tang, J.Q. Wu, C.H. Xu, Thermal-conductivity studies of macro-porous polymer-derived SiOC ceramics, Int. J. Thermophys. 35 (2014) 76–89.
[31] J.K. Carson, S.J. Lovatt, D.J. Tanner, A.C. Cleland, Thermal conductivity bounds for isotropic, porous materials, Int. J. Heat Mass Transf. 48 (2005) 2150–2158.
[32] D.S. Smith, A. Alzina, J. Bourret, B. Nait-Ali, F. Pennec, N. Tessier-Doyen, K. Otsu, H. Matsubara, P. Elser, U.T. Gonzenbach, Thermal conductivity of porous materials, J. Mater. Res. 28 (17) (2013) 2260–2272.
[33] K.E. Pappacena, K.T. Faber, H. Wang, W.D. Porter, Thermal conductivity of porous silicon carbide derived from wood precursors, J. Am. Ceram. Soc. 90 (9) (2007) 2855–2862.
[34] H.X. Zhang, C.B. Fidelis, A.L. Serva, M. Wilhelm, K. Rezwan, Water-based freeze casting: adjusting hydrophobic polymethylsiloxane for obtaining hierarchically ordered porous SiOC, J. Am. Ceram. Soc. 100 (2017) 1907–1918.
[35] H.M. Liu, D. Xu, P. Xu, R.J. Huang, X.D. Xu, L.F. Li, L.H. Gong, Dismountable sample holder apparatus for rapid thermal conductivity measurements based on cryocooler, AIP Conf. Proc. 1434 (2012) 1363–1370.
[36] M. Scheffler, T. Gambaryan-Roisman, T. Takahashi, J. Kaschta, H. Muenstedt, P. Buhler, P. Greil, Pyrolytic decomposition of preceramic organo polysiloxanes, Ceram. Trans. 115 (2002) 239–250.
[37] A. Saha, R. Raj, D.L. Williamson, A model for the nanodomains in polymer derived SiCO, J. Am. Ceram. Soc. 89 (2006) 2188–2195.
[38] S. Deville, E. Saiz, A.P. Tomsia, Ice-templated porous alumina structures, Acta Mater. 55 (2007) 1965–1974.
[39] R.O. Ritchie, The conflicts between strength and toughness, Nat. Mater. 10 (2011) 817–822.
[40] C. Kittel, Interpretation of the thermal conductivity of glasses, Phys. Rev. 75 (6) (1949) 972–974.
[41] A. Gurlo, E. Ionescu, R. Riedel, D.R. Clarke, The thermal conductivity of polymer-derived amorphous Si–O–C compounds and nano-composites, J. Am. Ceram. Soc. 99 (1) (2016) 281–285.
[42] D.B. Marshall, M.R. Jarnes, J.R. Porter, Structural and mechanical property changes in toughened magnesia-partially-stabilized zirconia at low temperatures, J. Am. Ceram. Soc. 72 (2) (1989) 218–227.
[43] W.J. Xue, T. Ma, Z.P. Xie, J. Yi, Research into mechanical properties of reaction-bonded SiC composites at cryogenic temperatures, Mater. Lett. 65 (2011) 3348–3350.
[44] W.W. Wu, J.Y. Gui, S. Wei, W.J. Xue, Z.P. Xie, Si_3N_4-SiCw composites as structural materials for cryogenic application, J. Eur. Ceram. Soc. 36 (2016) 2667–2672.
[45] S. Wei, Z.P. Xie, W.J. Xue, J.Y. Gui, J. Chen, How does pore-induced crack change as temperatures decrease from 293 K to 77 K, Ceram. Int. 41 (2015) 15246–15249.
[46] J. Tan, G. Wang, Z.Y. Liu, J. Bednarčík, Y.L. Gao, Q.J. Zhai, N. Mattern, J. Eckert, Correlation between atomic structure evolution and strength in a bulk metallic glass at cryogenic temperature, Sci Rep 4 (3897) (2014) 1–7.
[47] F.C. Hull, S.K. Hwang, J.M. Wells, R.I. Jaffee, Effect of composition on thermal expansion of alloys used in power generation, J. Mater. Eng. 9 (1987) 81–92.
[48] C. Dellacorte, J.A. Fellenstein, The effect of compositional tailoring on the thermal expansion and tribological properties of PS300: a solid lubricant composite coating, Tribol. Trans. 40 (4) (1997) 639–642.
[49] G.K. White, Thermal expansion of reference materials: copper, silica and silicon, J. Phys. D. Appl. Phys. 6 (1973) 2070–2078.
[50] F.C. Marques, R.G. Lacerda, A. Champi, V. Stolojan, D.C. Cox, S.R.P. Silva, Thermal expansion coefficient of hydrogenated amorphous carbon, Appl. Phys. Lett. 83 (2003) 3099–3101.
[51] S. Ghabezloo, Effect of porosity on the thermal expansion coefficient: A discussion of the paper 'Effects of mineral admixtures on the thermal expansion properties of hardened cement paste' by Z.H. Shui, R. Zhang, W. Chen, D. Xuan, Constr. Build. Mater. 24 (9) (2010) 1761–1767, Constr. Build. Mater. 24 (2010) 1796–1798.
[52] G.M. Renlund, S. Prochazka, R.H. Doremus, Silicon oxycarbide glasses, 2. Structure and properties, J. Mater. Res. 6 (1991) 2723–2734.
[53] T. Rouxel, G. Massouras, G.-D. Sorarù, High temperature behavior of a gel-derived SiOC glass: elasticity and viscosity, J. Sol-Gel Sci. Technol. 14 (1999) 87–94.
[54] R.L. Coble, W.D. Kingery, Effect of porosity on physical properties of sintered alumina, J. Am. Ceram. Soc. 39 (1956) 377–385.
[55] N. Khalili, A. Uchaipichat, A.A. Javadi, Skeletal thermal expansion coefficient and thermo-hydro-mechanical constitutive relations for saturated homogeneous porous media, Mech. Mater. 42 (2010) 593–598.
[56] A.L. Sutton, V.C. Howard, The role of porosity in the accommodation of thermal expansion in graphite, J. Nucl. Mater. 7 (1962) 58–71.
[57] J.A. Kuszyk, R.C. Bradt, Influence of grain size on effects of thermal expansion anisotropy in $MgTi_2O_5$, J. Am. Ceram. Soc. 56 (1973) 420–423.
[58] Z.H. Karadeniz, D. Kumlutas, A numerical study on the coefficients of thermal expansion of fiber reinforced composite materials, Compos. Struct. 78 (2007) 1–10.
[59] M. Nakata, K. Suganuma, Effect of internal structure on thermal properties of alumina/aluminum composites fabricated by gelate-freezing and partial-sintering process, respectively, Mater. Trans. 46 (2005) 130–135.
[60] E.H. Kerner, The elastic and thermo-elastic properties of composite media, Proc. Phys. Soc. B 69 (1956) 808–813.
[61] R.A. Schapery, Thermal expansion coefficients of composite materials based on energy principles, J. Compos. Mater. 2 (1968) 380–404.
[62] H. Nakajima, Fabrication, properties and application of porous metals with directional pores, Prog. Mater. Sci. 52 (2007) 1091–1173.

[63] R.C. Zeller, R.O. Pohl, Thermal conductivity and specific heat of noncrystalline solids, Phys. Rev. B 4 (1971) 2029–2041.

[64] K.M. Kim, S.H. Jang, Y.W. Kim, W.S. Seo, Thermal and mechanical properties of SiC–$TiC_{0.5}N_{0.5}$ composites, J. Am. Ceram. Soc. 98 (2) (2015) 616–623.

[65] I.H. Tavman, Effective thermal conductivity of granular porous materials, Int. Commun. Heat Mass Transfer 23 (2) (1996) 169–176.

[66] R. Landauer, The electrical resistance of binary metallic mixtures, J. Appl. Phys. 23 (1952) 779–784.

[67] J.F. Wang, J.K. Carson, M.F. North, D.J. Cleland, A new approach to modelling the effective thermal conductivity of heterogeneous materials, Int. J. Heat Mass Transf. 49 (2006) 3075–3083.

[68] H.W. Russell, Principles of heat flow in porous insulators, J. Am. Ceram. Soc. 18 (1935) 1–5.

[69] C. Ferraro, E. Garcia-Tuñon, V.G. Rocha, S. Barg, M.D. Fariñas, T.E.G. Alvarez-Arenas, G. Sernicola, F. Giuliani, E. Saiz, Light and strong SiC networks, Adv. Funct. Mater. 26 (2016) 1636–1645.

[70] Y. Grebenyuk, H.X. Zhang, M. Wilhelm, K. Rezwan, M.E. Dreyer, Wicking into porous polymer-derived ceramic monoliths fabricated by freeze-casting, J. Eur. Ceram. Soc. 37 (2016) 1993–2000.

[71] B. Weisenseel, P. Greil, T. Fey, Biomorphous silicon carbide as novel loop heat pipe wicks, Adv. Eng. Mater. 19 (2016) 1–9.